



# Synthesis of Fe-doped WO<sub>3</sub> nanostructures with high visible-light-driven photocatalytic activities



Hui Song, Yaguang Li, Zirui Lou, Mu Xiao, Liang Hu, Zhizhen Ye, Liping Zhu \*

State Key Laboratory of Silicon Materials, Department of Materials Science and Engineering, Zhejiang University, Zheda Road 38, Hangzhou 310027, People's Republic of China

## ARTICLE INFO

### Article history:

Received 5 September 2014

Received in revised form 27 October 2014

Accepted 8 November 2014

Available online 15 November 2014

### Keywords:

Fe-doped WO<sub>3</sub>

Nanostructures

Photocatalysts

Visible-light absorption

DFT

## ABSTRACT

In this paper, the Fe-doped WO<sub>3</sub> nanostructures with precisely controlled Fe doping contents are obtained by using a template method. The characterizations obviously show that the as-prepared samples have hollow spherical like morphology, small grain size (10 nm), high crystalline quality, and ultrahigh surface area (225 m<sup>2</sup>/g). Furthermore, the band gap of the Fe-doped WO<sub>3</sub> nanostructures is facily tunable by controlling the Fe contents. And the density-functional theory (DFT) calculation reveals that the formation of impurity band in the band gap narrows the band gap of the Fe-doped WO<sub>3</sub> nanostructures. The photocatalytic activity of WO<sub>3</sub> nanostructures could be remarkably enhanced by doping the Fe impurity. This can be attributed to the fact that the red shift of absorption edge and the trapping effect of the Fe-doped WO<sub>3</sub> nanostructures. The research result provides a general and effective method to synthesize different photocatalysts with enhanced visible-light-driven photocatalytic performance.

© 2014 Elsevier B.V. All rights reserved.

## 1. Introduction

Nowadays, environmental pollution is an extremely serious problem [1]. As one of the most valid and promising techniques, semiconductor photocatalysts can utilize solar energy or artificial indoor illumination to decompose the pollutants and have been received widespread attention [2]. Tungsten oxide (WO<sub>3</sub>) is one of the best photocatalysts which has outstanding stability, good electron transport properties, no-photo-corrosion and high photoactivity [3–5]. However, as a relatively wide band gap photocatalyst (2.8–3.0 eV) [6], the WO<sub>3</sub> is only excited by the blue and near ultraviolet regions of the solar spectrum. Thus, in order to increase the photocatalytic performance of WO<sub>3</sub>, narrowing the band gap is the main theme of the WO<sub>3</sub> photocatalysis. The band gap of WO<sub>3</sub> could be effectively reduced by doping various elements [7–9]. A variety of metal elements such as Mg, Zn, Fe, Mo, V and Ti have been applied to tune the band gap and improve the photocatalytic performance of WO<sub>3</sub> [10–16]. Especially, due to the enhancement of the absorption of visible light and effective separation and transformation of the photo-excited electrons and holes,

Fe element has gained more and more attention in narrowing the band gap of WO<sub>3</sub> [17,18].

On the other hand, tuning the morphology and structure of photocatalytic materials is the important way to enhance the photocatalytic efficiency of photocatalytic materials [19–21]. Many reports have demonstrated that the nanostructures with dimensions comparable or smaller than 10 nm could remarkably improve the photocatalytic performance of the materials [22,23]. It is widely believed that the smaller the grain size the larger the specific surface area. In addition, the diffusion length for photo-excited electrons and holes in grains is shortened, when the grain size becomes smaller. It is beneficial to decrease the recombination of the photo-excited electrons, thereby, improving the photocatalytic performance [24–26].

In this work, we present a novel and simple method for preparing the Fe-doped WO<sub>3</sub> nanostructures with the assistance of carbon colloidal spheres. We found that the Fe-doped WO<sub>3</sub> nanostructures have the small grain size in 10 nm scale and ultrahigh surface area of 225 m<sup>2</sup>/g. Furthermore, the band gap of the Fe-doped WO<sub>3</sub> is facily tunable by controlling the Fe doped contents. The photocatalytic performance of Fe-doped WO<sub>3</sub> nanostructures was evaluated by the photocatalytic decomposition of RhB under visible light ( $\lambda > 420$  nm) lighting. It is revealed that the Fe-doped WO<sub>3</sub> nanostructures exhibit superior visible-light-driven photocatalytic activity. As far as we know, this is the first time to report the preparation of Fe-doped WO<sub>3</sub> nanostructures.

\* Corresponding author. Tel.: +8657187951958; fax: +86 571 87952625.  
E-mail address: [zlp1@zju.edu.cn](mailto:zlp1@zju.edu.cn) (L. Zhu).

## 2. Experimental

### 2.1. Materials synthesis

The carbon spheres were hydrothermally synthesized using the method reported by Li et al. [27]. To synthesize the Fe-doped  $\text{WO}_3$  nanostructures, analytical-grade tungsten hexachloride ( $\text{WCl}_6$ , 1 mmol) and stoichiometric amount of iron(III) nitrate nonahydrate ( $\text{Fe}(\text{NO}_3)_3 \cdot 9\text{H}_2\text{O}$ ) were dissolved in 100 mL of *N,N*-dimethylformamide. A dispersion of the as-prepared carbon spheres (50 mg) was added to the above solution, and the reaction was sonicated for 30 min. The as-obtained mixture solution was stirred at room temperature for 24 h. The precipitate was filtered, rinsed with distilled water and ethanol, and dried in an oven in air at  $80^\circ\text{C}$  for 6 h. The Fe-doped  $\text{WO}_3$  nanostructures were obtained by annealing the products in air at  $400^\circ\text{C}$  for 6 h. The continuously variable concentrations of Fe in Fe-doped  $\text{WO}_3$  nanostructures could be attempted by controlling the ratio of  $\text{WCl}_6$  and  $\text{Fe}(\text{NO}_3)_3 \cdot 9\text{H}_2\text{O}$  (1:0, 4:1, 2:1, 1:1, 3:4, 3:5) in the solution. The contents of Fe in  $\text{WO}_3$  were 0, 1.14, 3.16, 5.25, 7.08 and 9.32% by molar ratio. The corresponding products were marked as S1, 2, 3, 4, 5 and 6, respectively.

### 2.2. Materials characterization

The crystallographic structure of the as-prepared photocatalysts was characterized by the powder X-ray diffraction. The scanning electron microscopy (SEM; S-4800, Hitachi) and transmission electron microscopy (HR-TEM, FEI F20) were used to identify the morphology and crystal structure of the samples. The XPS spectra were recorded on a Thermo ESCALAB-250 spectrometer using a monochromatic Al  $K\alpha$  radiation source (1486.6 eV). The binding energies determined by X-ray photoelectron spectroscopy (XPS) were corrected by reference to the adventitious carbon peak (285.0 eV) for each sample. The optical properties were tested on a Shimadzu UV3600 ultraviolet-visible spectrophotometer.

### 2.3. Photocatalytic test

The photocatalytic performances of the samples were evaluated by the photodecomposition of RhB under visible light from a 300 W Xe lamp furnished with a 420 nm cutoff filter. In each experiment, the photocatalysts (30 mg) were poured into 100 mL of RhB solution (20 mg/L) or 100 mL of phenol solution (20 mg/L). The suspension was stirred in the dark for 5 h to obtain a good adsorption-desorption equilibrium between the organic molecules and the catalyst surfaces. The temperature of the suspension was maintained at room temperature by circulating water, and the system was open to the air. Then the measurement of RhB or phenol degradation was carried out on a UV-vis spectroscopy (Shimadzu UV3600).

## 3. Computational details

All the calculations were carried out using the density functional theory (DFT) based on the commercial version of the software package CASTEP (Cambridge Sequential Total Energy Package), which could offer the vibrational properties of adsorption and accurate calculations of energy [28]. The exchange-correlation effects and core electrons were taken into account via the local-density approximation (LDA) and the generalized gradient approximation (GGA). We considered Fe doping effects using  $1 \times 1 \times 2$  monoclinic supercell (16 W atoms and 48 O atoms) and substituted one W atom by Fe atom, resulting in a 6.25% Fe concentration. All the plane waves kinetic energy cut-off were set to 340 eV. The mechanical equilibrium was accomplished by conjugate gradient minimization

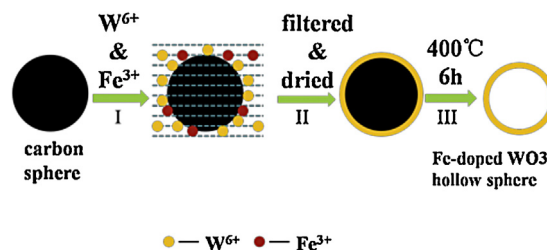


Fig. 1. Schematic illustration of the formation of Fe-doped  $\text{WO}_3$  hollow nanospheres.

of the forces to a tolerance of  $5 \times 10^{-2}$  eV/Å, and the atomic positions to a tolerance of  $2 \times 10^{-3}$  Å, the total energy to a tolerance of  $2 \times 10^{-6}$  eV.

## 4. Results and discussion

### 4.1. Synthesis process

The high quality Fe-doped  $\text{WO}_3$  nanostructures were prepared through a simple method using the carbon colloidal spheres as hard templates. The synthesis of Fe-doped  $\text{WO}_3$  nanostructures were schematically illustrated in Fig. 1. In step I, the  $\text{W}^{6+}$  and  $\text{Fe}^{3+}$  with different ratio could be absorbed on the surface of carbon spheres, hence obtained the carbon spheres@W-/Fe-precursor core shell nanospheres. In our method, the templates had large numbers of  $-\text{OH}$  and  $-\text{C}=\text{O}$  groups on their surface [29] and the W and Fe ions were homogeneously absorbed at an atomic scale in the surface of the carbon spheres. Therefore, an evenly Fe-doped  $\text{WO}_3$  hollow nanosphere could be obtained by calcining the carbon spheres@W-/Fe-precursor core shell nanospheres in air at  $400^\circ\text{C}$  for 6 h. The calcination temperature ( $400^\circ\text{C}$  for 6 h) is a very important factor in the synthesis of Fe-doped  $\text{WO}_3$ . If the calcination temperature is too low, templates are difficult to remove or take a long time. On the other hand, the iron oxides will precipitate in the Fe-doped  $\text{WO}_3$  system when the calcination temperature is higher than  $500^\circ\text{C}$ . Thus, the calcination temperature is fixed at  $400^\circ\text{C}$ . The average concentrations of Fe in the  $\text{WO}_3$  nanostructures were measured by the energy-dispersive X-ray spectroscopy (EDX) (Fig. S1 in the Supporting information). It revealed that the Fe concentrations of the samples could be tuned from 0 to 9.32% gradually (Table 1).

### 4.2. X-ray diffraction study

The crystallographic structure of the products was characterized by X-ray diffraction (XRD). The XRD spectra of the pure  $\text{WO}_3$  and Fe-doped  $\text{WO}_3$  prepared were shown in Fig. 2. The XRD

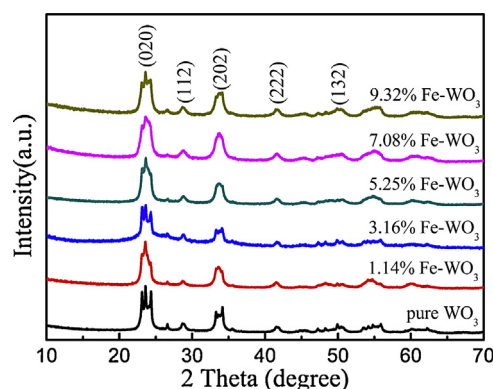


Fig. 2. XRD patterns of the as-prepared samples.

**Table 1**  
Physicochemical properties and photocatalytic performances of as-prepared.

Sample	Average Fe content (at.%) <sup>a</sup>	Surface Fe content (at.%) <sup>b</sup>	Surface area (m <sup>2</sup> /g)	Band gap (eV)	Rate constant $k_{\text{RhB}}$ ( $\times 10^{-3} \text{ min}^{-1}$ )	Rate constant $k_{\text{phenol}}$ ( $\times 10^{-3} \text{ min}^{-1}$ )
S1	0.00	0.00	201	3.10	0.76	0.42
S2	1.14	2.21	212	3.04	2.28	0.99
S3	3.16	6.57	209	2.90	7.38	3.67
S4	5.25	14.83	225	2.78	21.47	9.55
S5	7.08	19.02	232	2.67	11.22	5.81
S6	9.32	20.98	216	2.58	5.09	2.38

<sup>a</sup> Measured by the energy-dispersive X-ray spectroscopy (EDX).

<sup>b</sup> Measured by the X-ray photoelectron spectroscopy (XPS).

pattern of pure WO<sub>3</sub> nanostructures were in readily agreement with the XRD pattern of monoclinic phase WO<sub>3</sub> (PDF#43-1035) with the lattice constants of  $a=0.7297 \text{ nm}$ ,  $b=0.7539 \text{ nm}$ ,  $c=0.7688 \text{ nm}$ , and  $\beta=90.91^\circ$ . With the increasing Fe contents, no apparent peaks of iron oxides or other phases could be detected in the doped products, suggesting that the existence of Fe in the product hardly affect the crystallization properties of tungsten oxide. This could be attributed to the fact that the Fe concentrations were a little low and the radius of Fe<sup>3+</sup> (0.64 Å) and the radius of W<sup>6+</sup> (0.62 Å) are nearly equal. Thus, the Fe<sup>3+</sup> ions could be doped into the crystal lattice of WO<sub>3</sub>, forming an iron–tungsten finite solid solution. The broadening of the diffraction peaks could be ascribed to the small size of the nanograins.

#### 4.3. Raman spectra study

To further obtain more structural and bonding environment information about the Fe-doped WO<sub>3</sub>, the Raman spectra of all samples were performed. As shown in Fig. 3, pure WO<sub>3</sub> only contained the characteristic peaks of the monoclinic phase, which was consistent with the result of XRD. The peaks at 805 cm<sup>−1</sup> and 270 cm<sup>−1</sup> were ascribed to the stretching vibration of O–W–O bonds and the bending vibration of O–W–O bonds [13], respectively. Upon iron doping, no other peaks corresponding to the modes of the Fe–O bonds in all products could be observed, corresponding with the results of XRD. Remarkably, the characteristic peaks of the products were gradually broadened and shifted to lower wavenumbers with the increase of iron contents, which may be result from iron occupying the substitutional site in WO<sub>3</sub>.

#### 4.4. Morphology and structure of Fe-doped WO<sub>3</sub> nanostructures

The SEM patterns of the as-prepared samples with different Fe contents were shown in Fig. 4. All the products possessed a spherical like morphology with diameters ranging from 150 to 250 nm. And the morphology of the samples was not changed with the

increasing of Fe contents. The SEM images indicated that the shell of the spheres was composed of nanoparticles with small size. Furthermore, there were many pores on the surface of the hollow nanospheres, which could act as the transport channels for many molecules involved in the reaction or increase the absorption of light and consequently enhanced the photocatalytic performance.

In order to further study the morphology and crystal structure of the as-prepared samples, the TEM and HRTEM images of the samples were shown in Fig. 5. The TEM image of Fe-doped WO<sub>3</sub> hollow nanospheres shown in Fig. 5a and b clearly demonstrated that the thickness of the shell was about 10 nm and large numbers of pores were existed in the shell. Meanwhile, Fig. 5c and d displayed the HRTEM image of pure WO<sub>3</sub> and 5.25% Fe-doped WO<sub>3</sub>. It could be seen that the size of particles comprised the shell was about 10 nm. Besides, the HRTEM image (Fig. 5c) of pure WO<sub>3</sub> suggested that the sample has a well-defined crystalline structure. The inter-planar spacing of pure WO<sub>3</sub> was calculated to be 0.378 nm, indexing to the (020) crystal plane of the WO<sub>3</sub> structure. Furthermore, the inter-planar spacing observed in the 5.25% Fe-doped WO<sub>3</sub> (Fig. 5d) was nearly equal to the inter-planar spacing of pure WO<sub>3</sub>, which was consistent with the XRD results.

#### 4.5. X-ray photoelectron spectroscopy study

To investigate the chemical composition of Fe-doped WO<sub>3</sub> and determine the chemical status of Fe elements in the doped products, the samples were measured by XPS (X-ray photoelectron spectroscopy). Fig. 6a presented the overview of XPS spectrum of 5.25% Fe-doped WO<sub>3</sub>. It showed that the doped products contain C, W, O and Fe elements and theirs corresponding photoelectron peaks were C1s, W4f, O1s and Fe2p, respectively. Fig. 6b showed the W4f core level XPS spectrum of the doped product. There were two peaks in this spectrum corresponding to W4f<sub>7/2</sub> and W4f<sub>5/2</sub> with values of 35.6 eV and 37.6 eV, respectively, which were consistent with the corresponding XPS spectra reported in the literatures [7–9]. So it could be considered that W element in the products existed in the form of W<sup>6+</sup> ions. The high resolution XPS spectrum of the Fe2p was exhibited in Fig. 6c. The peak of the Fe2p at 711.4 eV could be attributed to 2p<sub>3/2</sub> of Fe<sup>3+</sup> ions [18]. This peak value was distinct from that of Fe<sup>3+</sup> in Fe<sub>2</sub>O<sub>3</sub> (at 710.7 eV) [30]. The difference of Fe 2p<sub>3/2</sub> level binding energy may be owing to the substitution of Fe<sup>3+</sup> for W<sup>6+</sup> in Fe-doped WO<sub>3</sub> and the formation of W–O–Fe bonds in the product. Fig. 6d depicted the O1s core level binding of the doped samples. The O 1s XPS spectrum could be fitted into distinct components, demonstrating that different kinds of O binding states were existed in Fe-doped WO<sub>3</sub> nanostructures. The predominant peak was assigned to the crystal lattice oxygen (Fe–O and W–O). Furthermore, the exact contents of surface Fe elements in the samples were characterized by XPS and the results were listed in Table 1. Obviously, the surface Fe contents were higher than the average content characterized by EDX. Therefore, it was clearly that Fe elements mainly accumulated in the surface layer, which was beneficial to enhance photocatalytic performance [31].

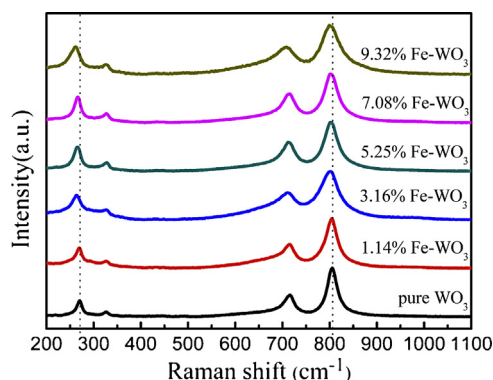


**Fig. 3.** Raman spectra of the as-prepared samples.

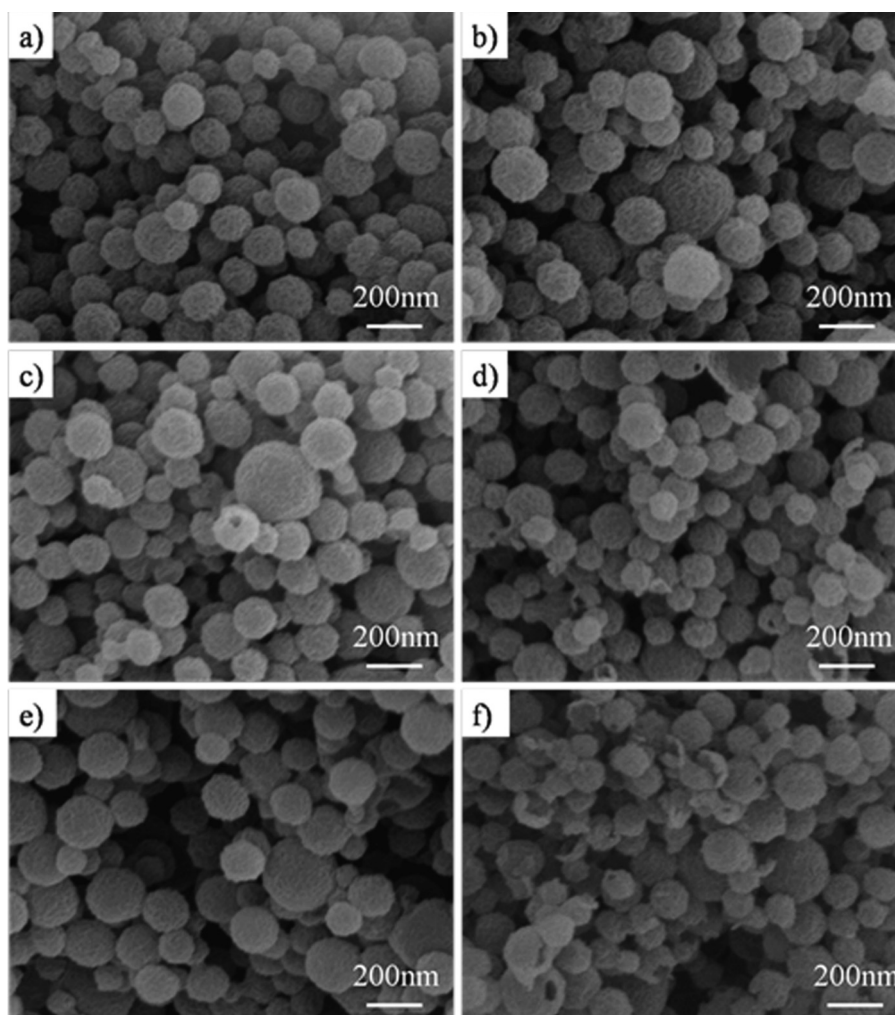


**Fig. 4.** (a), (b), (c), (d), (e) and (f) are the SEM images of the as-prepared S1, S2, S3, S4 and S5, respectively.

#### 4.6. UV-vis spectroscopy

The UV-vis diffuse reflectance spectra of the samples were shown in Fig. 7. These products exhibited absorption in both UV and visible-light regions. Obviously, the diffuse reflectance spectra of all Fe-doped  $\text{WO}_3$  nanostructures displayed a red shift and increased absorption in the visible-light range. The higher iron content, the greater the degree of red shift. Besides, the band gap of the samples could be confirmed by the formula  $\alpha h\nu = A(h\nu - E_g)^{n/2}$ , where  $\alpha$ ,  $h$ ,  $\nu$ ,  $A$ ,  $E_g$  and  $n$  are the absorption coefficient, Planck constant, incident light frequency, a constant, band gap and an integer, respectively [32]. For  $\text{WO}_3$ , the value of  $n$  which depends on the characteristics of optical the transition is 4 [33]. By calculation, the band gap of the samples was listed in Table 1. As we seen, with the increasing of Fe contents, the band gap of the samples decreased gradually. This was due to the fact that the doping Fe ions could create a donor level above the original valence band of  $\text{WO}_3$  to narrow the  $\text{WO}_3$  band gap. Thus, these results demonstrated that the Fe ions were indeed incorporated into the lattice of  $\text{WO}_3$ .

#### 4.7. BET surface areas and pore distributions

Nitrogen adsorption-desorption isotherms at 77 K and corresponding pore diameter distribution curves (inset) from the desorption branch by the BJH method of the 5.25% Fe-doped  $\text{WO}_3$

were plotted Fig. 8. The isotherms of the Fe-doped  $\text{WO}_3$  nanostructures could be categorized as a typical type IV [34], with distinct hysteresis loops observed in the relative pressure range of 0.6–1.0. It was clearly indicated that the products were mesoporous materials, which agreed well with the morphologies and microstructures of porous  $\text{WO}_3$  products (Fig. 5). Furthermore, the BET surface areas of the S4 were calculated to be  $225 \text{ m}^2/\text{g}$ . Moreover, the pore diameter distribution of the sample indicated that the average pore diameter was about 16 nm. The other products had similar isotherm and pore diameter distribution and theirs BET surface areas were listed in Table 1. Obviously, the BET surface areas of the as-prepared samples were similar. This may be because the use of the template was the same and they all had the same monolayer nanostructure. Such nanoporous structures and large BET surface areas were crucial for photocatalysts, since they could supply transport channels for the molecules involved in the reaction and effectively separate photo-excited electron-hole pairs, reducing the recombination of electron-hole pairs [35].

#### 4.8. Photocatalytic activity

The photocatalytic activity of the as-synthesized samples were investigated by degrading a Rhodamine-B (RhB) and phenol aqueous solution under visible light irradiation ( $\lambda > 420 \text{ nm}$ ) using a 300 W Xe lamp. In order to study the impact of the contents of



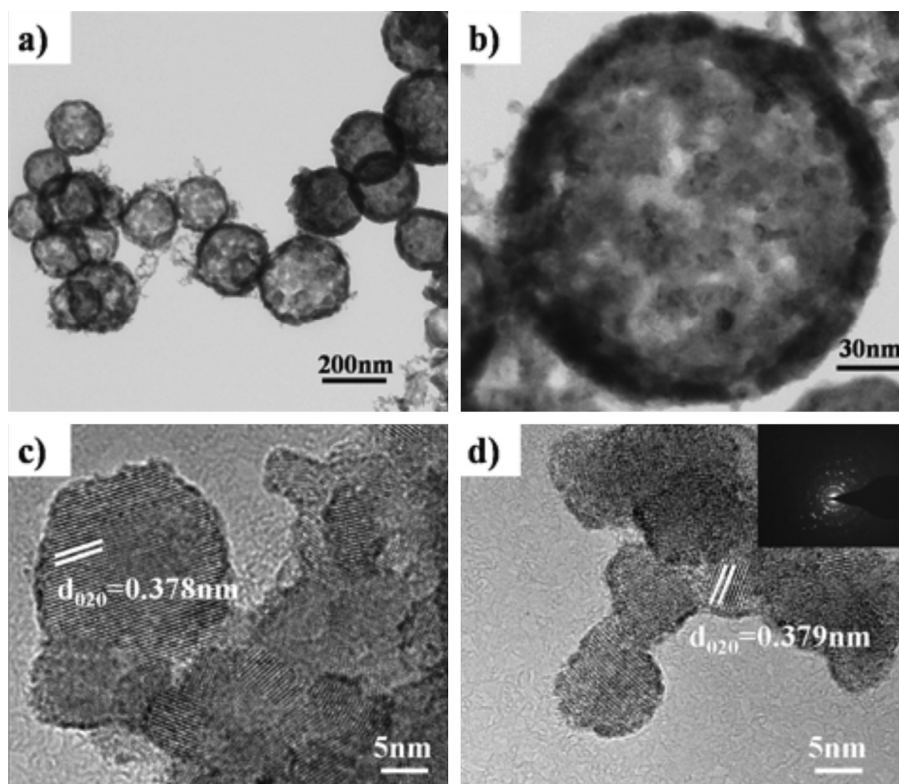


**Fig. 5.** (a) and (b) are the low-magnification TEM image and high-magnification TEM image of S4, respectively; (c) and (d) are the HRTEM images of S1 and S4, respectively, inset in Fig. 5d is the corresponding SAED pattern of the sample.

Fe on the photocatalytic performance, a series of comparative tests were researched.

The changes of the RhB concentration for samples with different contents of Fe were shown in Fig. 9a. With the catalyst without light or without any catalyst, RhB was almost not degraded. The pure  $\text{WO}_3$  hollow nanospheres possessed an inferior

photocatalytic performance under visible-light illumination due to the large band gap of 3.10 eV, contrastively Fe-doped  $\text{WO}_3$  hollow nanospheres presented much higher performance than pure  $\text{WO}_3$  hollow nanospheres. With the increasing of Fe contents, the photocatalytic performances of the products increased speedily and had a downtrend with further increasing Fe contents. Compared

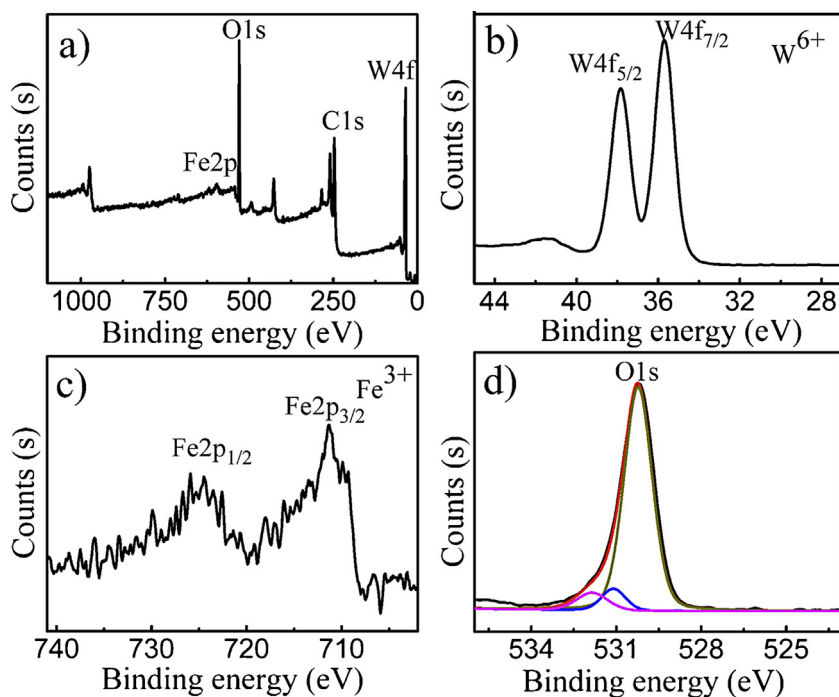


**Fig. 6.** (a), (b), (c) and (d) are the XPS spectra of S4 for an overview XPS spectrum, W4f spectrum, Fe2p spectrum and O1s spectrum.

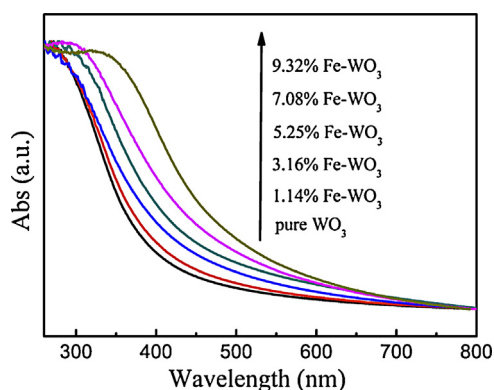


Fig. 7. UV-vis diffuse absorption spectra of the as-prepared samples.

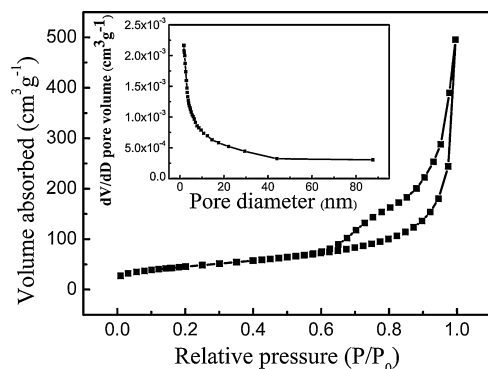


Fig. 8. Nitrogen adsorption-desorption isotherms and corresponding pore diameter distribution curves (inset) of S4.

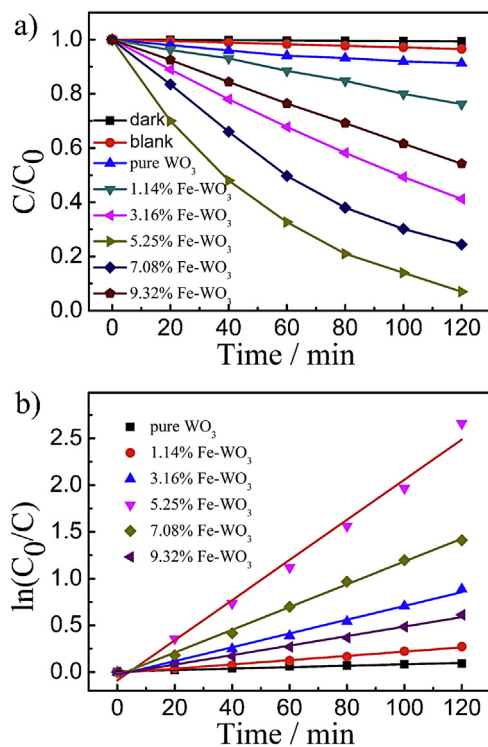


Fig. 9. (a) Photodegradation of RhB by pure  $\text{WO}_3$  and Fe-doped  $\text{WO}_3$  under visible light. (b) The corresponding first-order kinetics plot.

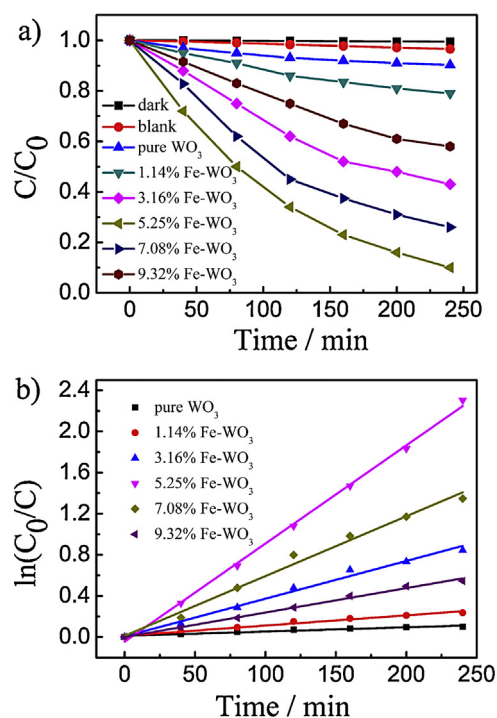
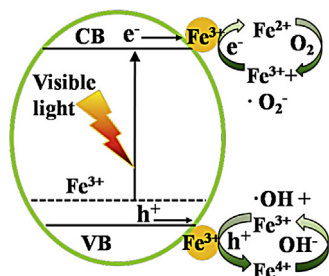


Fig. 10. (a) Photodegradation of phenol by pure  $\text{WO}_3$  and Fe-doped  $\text{WO}_3$  under visible light. (b) The corresponding first-order kinetics plot.

with other samples, the sample with 5.25% Fe concentrations presented the highest photocatalytic performance. Furthermore, the linear profile indicated that photocatalytic degradation kinetics of RhB could be approximated by the pseudo-first-order rate law and were presented in Fig. 9b. The first-order rate constant ( $k$ ) were calculated by the equation:  $\ln(C_0/C) = k\tau$ , where  $C_0$  and  $C$  are the concentration of RhB in aqueous solution at times 0 and  $\tau$ , and  $\tau$  is the time of irradiation [36]. The calculated results were listed in Table 1. The value of rate constant  $k_{\text{RhB}}$  of the sample presented the highest photocatalytic performance is  $0.02147 \text{ min}^{-1}$ , which was 28 times higher than pure  $\text{WO}_3$  ( $k_{\text{RhB}} = 0.00076 \text{ min}^{-1}$ ).

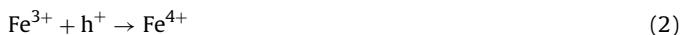
In addition to RhB, phenol was also selected as a representative model pollutant which has no light absorption characteristics in the visible light region. Fig. 10a showed the photodegradation efficiencies of phenol for the samples with different contents of Fe under visible-light illumination. The decrease of phenol concentration in the presence of pure  $\text{WO}_3$  was very small. However, the photocatalytic activities had been improved when  $\text{WO}_3$  was doped by Fe. About 93% of phenol was reduced in 240 min in the case of 5.25% Fe-doped  $\text{WO}_3$ . With the increasing of Fe contents, the photodegradation efficiencies were first increased and then decreased. Besides, the linear profile indicated that photocatalytic degradation kinetics of phenol was presented in Fig. 10b. And the values of rate constant  $k_{\text{phenol}}$  of the samples were listed in Table 1.

From the above results, we concluded that the photocatalytic performances of the Fe-doped  $\text{WO}_3$  hollow nanospheres have outstanding enhancements compared to the pure  $\text{WO}_3$  under visible-light illumination. In our case, the optimal Fe doping contents is 5.25%. And the photocatalytic performances of Fe-doped  $\text{WO}_3$  hollow nanospheres were decreased obviously when the Fe doping contents higher than 5.25%. There were several reasons for the above phenomenon. First, since the doping  $\text{Fe}^{3+}$  ions could create a donor level above the original valence band of  $\text{WO}_3$  to increase the absorption intensity of visible light [37]. The donor level was more and more distant from the valence band with the increasing of iron content. Therefore, huge numbers of electrons could be excited



**Fig. 11.** A schematic diagram of the charge separation and the photocatalytic activity for the Fe doped  $\text{WO}_3$  photocatalyst.

under visible light region, which could also efficiently enhance the photocatalytic performance. Second, if the Fe concentrations were lower than its optimal molar ratio,  $\text{Fe}^{3+}$  ions were mainly doped in the surface of the samples, which could be proved by the characterization of XPS.  $\text{Fe}^{3+}$  ions could trap and transfer electrons and holes to inhibit the recombination of photo-excited holes and electrons [18], which can be schematically shown in Fig. 11. And the detailed reaction steps are as follows:



To confirm the above effective charge separation mechanism in the Fe-doped  $\text{WO}_3$  photocatalyst, quenching experiments were performed using *tert*-butyl alcohol (BuOH) as  $\bullet\text{OH}$  scavenger [38], and ethylenediaminetetraacetic acid disodium salt (EDTA) as hole scavenger [39]. Fig. 12 showed the degradation rate of RhB under different condition using S4 (5.25% Fe- $\text{WO}_3$ ) as the photocatalyst. It was found that 93% (Fig. 12a) of RhB was degraded under visible light irradiation within 120 min. However, in the presence of BuOH and EDTA, the degradation rate was reduced to 25% (Fig. 12b) and 43% (Fig. 12c) under other identical condition, respectively. So, the photocatalytic degradation of RhB was mainly caused by  $\bullet\text{OH}$  radicals, which were mainly produced by  $\text{Fe}^{3+}$  and hole. And the addition of  $\bullet\text{OH}$  scavenger and hole scavenger made the  $\bullet\text{OH}$  radicals concentration decreased. Therefore, we can conclude that  $\text{Fe}^{3+}$  ions were beneficial to the separation of electron–hole pairs. However, if the amount of  $\text{Fe}^{3+}$  ions was too much, more and more  $\text{Fe}^{3+}$  ions were mainly doped at the major depth below the surface [37].  $\text{Fe}^{3+}$  ions usually act as recombination centers for the photo-excited electrons and holes, resulting in the decreasing of the photocatalytic performances [18].

Therefore, if the contents of Fe elements in  $\text{WO}_3$  were lower than its optimal molar ratio, with the increasing of Fe contents, the

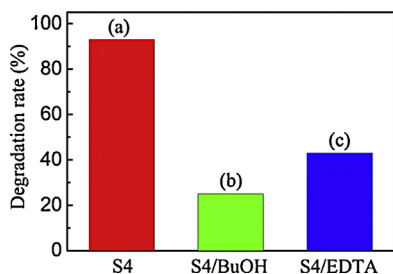


**Fig. 12.** Comparison of the degradation rates of RhB within 2 h using S4 (5.25% Fe-doped  $\text{WO}_3$ ) as photocatalyst under different conditions (RhB: 20 mg/L, 100 mL; BuOH: 3% (v/v); EDTA: 0.3 M).

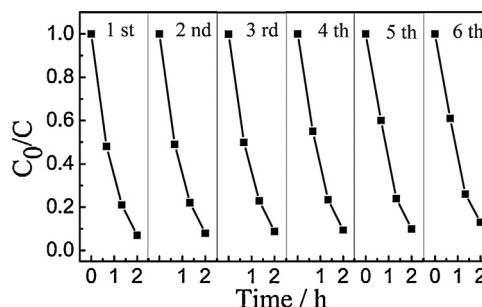


**Fig. 13.** Six cycles of the photo-degradation of RhB using S4 (5.25% Fe-doped  $\text{WO}_3$ ) as photocatalyst under visible-light irradiation for 120 min.

absorption intensity of visible light gradually increased and  $\text{Fe}^{3+}$  ions mainly existed in the surface of the samples to trap and transferred electrons and holes, thereby, increasing the photocatalytic efficiency gradually. However, the  $\text{Fe}^{3+}$  ions were mainly acting as recombination centers to decrease the photocatalytic efficiency, when the contents of Fe elements in  $\text{WO}_3$  higher than its optimal molar ratio. Hence, the photocatalytic efficiency was strongly related to the contents of Fe elements in  $\text{WO}_3$ .

We had further studied the stability and reusability of the as-prepared samples (S4) by collecting and reusing the same photocatalyst for six photocatalytic cycles (Fig. 13). Only a small loss in photocatalytic activity was observed, which might be partly caused by incomplete collection of the photocatalyst during each step. So the as-prepared samples showed excellent stability. Besides, we compared the photocatalytic efficiency of S4 with the photocatalytic efficiency of the hierarchical  $\text{WO}_3$  nanostructures in other literature [40–45] (Table S1 in the Supporting information), and found our result was much higher.

#### 4.9. DFT calculations

In order to study the effects of Fe elements on the band structure of monoclinic  $\text{WO}_3$ , the electronic properties of Fe-doped  $\text{WO}_3$  were studied by using the DFT (density functional theory) calculations. The monoclinic structure of  $(\text{Fe}_{1/16}\text{W}_{15/16})\text{O}_3$  unit cell was shown in Fig. S2 (in the Supporting information). And the total density of states (TDOS) plots of pure  $\text{WO}_3$  and  $(\text{Fe}_{1/16}\text{W}_{15/16})\text{O}_3$  were given in Fig. 14a and b, respectively. As shown in the TDOS plot of  $(\text{Fe}_{1/16}\text{W}_{15/16})\text{O}_3$ , the band gap of  $(\text{Fe}_{1/16}\text{W}_{15/16})\text{O}_3$  reduced obviously. Upon Fe doping, the valence band maximum (VBM) shifted up by about 0.4 eV while the conduction band minimum (CBM) diminished significantly due to the formation of a peak at 2 eV.

To analyze the change of band structure of  $(\text{Fe}_{1/16}\text{W}_{15/16})\text{O}_3$ , the partial density of states (PDOS) of pure  $\text{WO}_3$  and  $(\text{Fe}_{1/16}\text{W}_{15/16})\text{O}_3$  were plotted in Fig. 14c and d, respectively. The PDOS of pure  $\text{WO}_3$  in Fig. 14c showed that the valence band edge of pure  $\text{WO}_3$  was mainly dominated by the O 2p states, while its conduction band edge was predominantly composed of W 5d states with some contribution from O 2p states. As shown in Fig. 14d, the partially filled bands of  $(\text{Fe}_{1/16}\text{W}_{15/16})\text{O}_3$  were mainly from Fe 3d states and O 2p states. These O 2p states were hybridized with the neighboring Fe 3d states. Thus, the top edge of the valence band was consisted of Fe 3d states and O 2p states, which were near the Fe atom. Interestingly, the conduction band edge of  $(\text{Fe}_{1/16}\text{W}_{15/16})\text{O}_3$  was not dominated by W 5d states, but was dominated by O 2p states. This might be due to that the O 2p states were split and further electron interactions within the presence of Fe elements [46]. Therefore, the substitution of Fe atom for W atom in  $\text{WO}_3$  changed the CBM toward lower energy, and the VBM shifted upward, thereby, reducing the band gap. The calculated results could well explain the

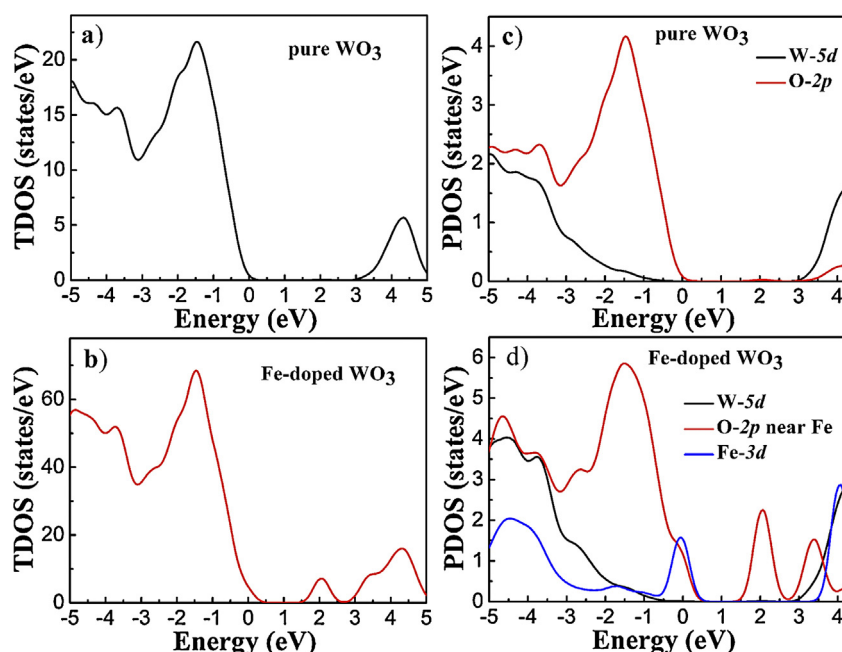


**Fig. 14.** (a) and (b) are the Total DOS of pure  $\text{WO}_3$  and  $(\text{Fe}_{1/16}\text{W}_{15/16})\text{O}_3$ ; (c) and (d) are the partial DOS of pure  $\text{WO}_3$  and  $(\text{Fe}_{1/16}\text{W}_{15/16})\text{O}_3$ . The Fermi levels for all of the DOS plots here are set to zero.

experimental phenomena that a red shift of the optical absorption edge in Fe-doped  $\text{WO}_3$  nanostructures.

## 5. Conclusion

In conclusion, we have prepared the Fe-doped  $\text{WO}_3$  nanostructures by using a template method and the Fe contents in  $\text{WO}_3$  nanostructures could be precisely controlled. The band gap of the Fe-doped  $\text{WO}_3$  could be tuned by controlling Fe doping contents. We found that the light absorption region could be broadened continually with the increasing of Fe doping content and the DFT calculation confirmed that the formation of impurity bands in the band gap could narrow the band gap of Fe-doped  $\text{WO}_3$ . What's more, the separation and transformation of the photo-excited electrons and holes could be enhanced with appropriate  $\text{Fe}^{3+}$  ions doping contents. Therefore, the Fe-doped  $\text{WO}_3$  nanostructures had the highest photocatalytic efficiency under visible light when it had 5 at.% Fe doping content. This research provides a general and effective method to synthesize different photocatalysts with enhanced visible-light-driven photocatalytic performance.

## Acknowledgements

This work was supported by National Natural Science Foundation of China 51372224, Program for Innovative Research Team in University of Ministry of Education of China (IRT13037), and National Science and Technology Support Program (2012BAC08B08).

## Appendix A. Supplementary data

Supplementary data associated with this article can be found, in the online version, at <http://dx.doi.org/10.1016/j.apcatb.2014.11.020>.

## References

- [1] G. Xi, J. Ye, Q. Ma, N. Su, H. Bai, C. Wang, *J. Am. Chem. Soc.* 134 (2012) 6508–6511.
- [2] H. Tong, S. Ouyang, Y. Bi, N. Umezawa, M. Oshikiri, J. Ye, *Adv. Mater.* 24 (2012) 229–251.
- [3] J. Cao, B. Luo, H. Lin, B. Xu, S. Chen, *Appl. Catal., B: Environ.* 111–112 (2012) 288–296.
- [4] Y. Peng, C. Liu, X. Zhang, J. Li, *Appl. Catal., B: Environ.* 140–141 (2013) 276–282.
- [5] A. Rey, P. García-Muñoz, M.D. Hernández-Alonso, E. Mena, S. García-Rodríguez, F.J. Beltrán, *Appl. Catal., B: Environ.* 154–155 (2014) 274–284.
- [6] B. Cole, B. Marsen, E. Miller, Y. Yan, B. To, K. Jones, M. Al-Jassim, *J. Phys. Chem. C* 112 (2008) 5213–5220.
- [7] Y. Liu, Y. Li, W. Li, S. Han, C. Liu, *Appl. Surf. Sci.* 258 (2012) 5038–5045.
- [8] Y. Sun, C.J. Murphy, K.R. Reyes-Gil, E.A. Reyes-García, J.M. Thornton, N.A. Morris, D. Raftery, *Int. J. Hydrogen Energy* 34 (2009) 8476–8484.
- [9] M. Takeuchi, Y. Shimizu, H. Yamagawa, T. Nakamuro, M. Anpo, *Appl. Catal., B: Environ.* 110 (2011) 1–5.
- [10] C. Feng, S. Wang, B. Geng, *Nanoscale* 3 (2011) 3695–3699.
- [11] A. Hameed, M.A. Gondal, Z.H. Yamani, *Catal. Commun.* 5 (2004) 715–719.
- [12] D.W. Hwang, J. Kim, T.J. Park, J.S. Lee, *Catal. Lett.* 80 (2002) 53–57.
- [13] K.M. Karuppasamy, A. Subrahmanyam, *J. Phys D: Appl. Phys.* 41 (2008) 035302.
- [14] Z.S. Seddigi, *Bull. Environ. Contam. Toxicol.* 84 (2010) 564–567.
- [15] X.C. Song, E. Yang, G. Liu, Y. Zhang, Z.S. Liu, H.F. Chen, Y. Wang, *J. Nanopart. Res.* 12 (2010) 2813–2819.
- [16] T. Tesfamichael, A. Ponzoni, M. Ahsan, G. Faglia, *Sens. Actuators, B: Chem.* 168 (2012) 345–353.
- [17] Z. Li, W. Shen, W. He, X. Zu, J. Hazard. Mater. 155 (2008) 590–594.
- [18] T. Tong, J. Zhang, B. Tian, F. Chen, D. He, J. Hazard. Mater. 155 (2008) 572–579.
- [19] X.W. Lou, L.A. Archer, Z. Yang, *Adv. Mater.* 20 (2008) 3987–4019.
- [20] Y. Liu, L. Yu, Y. Hu, C. Guo, F. Zhang, X. Wen David Lou, *Nanoscale* 4 (2012) 183–187.
- [21] Y. Liu, L. Zhou, Y. Hu, C. Guo, H. Qian, F. Zhang, X.W. Lou, *J. Mater. Chem.* 21 (2011) 18359.
- [22] Y. Lin, S. Zhou, S.W. Sheehan, D. Wang, *J. Am. Chem. Soc.* 133 (2011) 2398–2401.
- [23] Q. Wang, K. Zhu, N.R. Neale, A.J. Frank, *Nano Lett.* 9 (2009) 806–813.
- [24] C.B. Almquist, P. Biswas, *J. Catal.* 212 (2002) 145–156.
- [25] F. Amano, K. Nogami, M. Tanaka, B. Ohtani, *Langmuir* 26 (2010) 7174–7180.
- [26] K. Maeda, H. Terashima, K. Kase, K. Domen, *Appl. Catal., B: Gen.* 357 (2009) 206–212.
- [27] X. Sun, Y. Li, *Angew. Chem. Int. Ed.* 43 (2004) 597–601.
- [28] C. Lambert-Mauriat, V. Oison, *J. Phys.: Condens. Matter* 18 (2006) 7361–7371.
- [29] X. Sun, Y. Li, *Angew. Chem. Int. Ed.* 43 (2004) 3827–3831.
- [30] T. Yamashita, P. Hayes, *Appl. Surf. Sci.* 254 (2008) 2441–2449.
- [31] J. Yu, Q. Xiang, M. Zhou, *Appl. Catal., B: Environ.* 90 (2009) 595–602.
- [32] Z. Xie, Y. Zhu, J. Xu, H. Huang, D. Chen, G. Shen, *CrystEngComm* 13 (2011) 6393.
- [33] Y. He, Z. Wu, L. Fu, C. Li, Y. Miao, L. Cao, H. Fan, B. Zou, *Chem. Mater.* 15 (2003) 4039–4045.
- [34] Z.-G. Zhao, M. Miyauchi, *J. Phys. Chem. C* 113 (2009) 6539–6546.
- [35] M. Shang, W. Wang, H. Xu, *Cryst. Growth Des.* 9 (2008) 991–996.
- [36] Y. He, J. Cai, T. Li, Y. Wu, H. Lin, L. Zhao, M. Luo, *Chem. Eng. J.* 215–216 (2013) 721–730.
- [37] R. Dholam, N. Patel, M. Adami, A. Miotello, *Int. J. Hydrogen Energy* 34 (2009) 5337–5346.



- [38] K. Lv, Y. Xu, J. Phys. Chem. C 110 (2006) 6204–6212.
- [39] H. Zhang, R. Zong, Y. Zhu, J. Phys. Chem. C 113 (2009) 4605–4611.
- [40] G. Xi, B. Yue, J. Cao, J. Ye, Chem. Eur. J. 17 (2011) 5145–5154.
- [41] G.-H. He, C.-J. Liang, Y.-D. Ou, D.-N. Liu, Y.-P. Fang, Y.-H. Xu, Mater. Res. Bull. 48 (2013) 2244–2249.
- [42] D. Sánchez-Martínez, A. Martínez-de la Cruz, E. López-Cuellar, Mater. Res. Bull. 48 (2013) 691–697.
- [43] L. Zhang, X. Tang, Z. Lu, Z. Wang, L. Li, Y. Xiao, Appl. Surf. Sci. 258 (2011) 1719–1724.
- [44] X. An, J.C. Yu, Y. Wang, Y. Hu, X. Yu, G. Zhang, J. Mater. Chem. 22 (2012) 8525.
- [45] J. Huang, L. Xiao, X. Yang, Mater. Res. Bull. 48 (2013) 2782–2785.
- [46] M.N. Huda, Y. Yan, C.-Y. Moon, S.-H. Wei, M.M. Al-Jassim, Phys. Rev. B: Condens. Matter 77 (2008) 195102.